Hydrodynamic shape optimization of an autonomous and remotely-operated vehicle via a multi-surrogate model

Jian Liu*[1], Shanghua Wu[2], Xiufeng Yue[3], Qianjin Yue[1]

[1] State Key Laboratory of Structural Analysis for Industrial Equipment, Department of Engineering Mechanics, Dalian University of Technology, Dalian 116024, China
[2] School of Ocean Science and Technology, Dalian University of Technology, Panjin 124221, China
[3] School of Economics and Management, Dalian University of Technology, Dalian 116024, China

ARTICLE INFO

ABSTRACT

The design requirements for the hydrodynamic performance of underwater vehicles vary significantly depending on the application. Optimization without an initial model results in challenges such as large design domains, nonlinear complexity, and high data requirements. To optimize the hydrodynamic performance during the design process, in this paper, a multi-surrogate model was employed to progressively design the shape of an autonomous and remotely-operated vehicle. Based on the data characteristics of different stages, this approach strikes a balance among data quantity, prediction accuracy, and multi-objective requirements. An artificial neural network prediction surrogate model was constructed based on the principle of the minimum prediction factor using the optimal Latin hypercube sampling method. During the optimization of the design domain, the optimum objective was to minimize the dimensionless force ($G(x)$). During the multi-objective optimization stage, a regression kriging surrogate model was constructed based on a support vector product. The optimization objectives were to maximize volume and minimize dimensionless forces. This enabled the overall design process to attain optimal Pareto solutions within the design domain while simultaneously ensuring high prediction accuracy and minimum data requirements. The results obtained are consistent with the simulation comparison, thus verifying the reliability of the entire optimization process.

1. Introduction

Underwater vehicles play an important role in high-value commercial applications in ocean engineering, such as ocean exploration and surveying, engineering monitoring, intervention operation, and engineering maintenance [1–3]. Based on the control method, underwater vehicles can be broadly categorized into two types: Autonomous Underwater Vehicles (AUVs) and Remotely Operated Vehicles (ROVs) [4]. Currently, several new vehicles, such as Autonomous and Remotely-operated Vehicles (ARVs), Hybrid Remotely Operated Vehicles (HROVs), and Underwater Gliders (UGs), have been developed to meet particular engineering needs. [5–7].

---

* Corresponding author.

E-mail address: liujian_91ws@163.com

Underwater vehicles require precise control in complex environments. Therefore, improving the hydrodynamic performance of the main structure is important for most forms of underwater vehicles. Computational Fluid Dynamics (CFD) is considered to be the best tool for optimizing the shape of underwater vehicles under complex hydrodynamic environments [8]. Although ROVs consist of an integrated design of modules, they are often poorly designed in terms of the hydrodynamic performance. For AUVs with their own energy systems, resistance reduction is desirable because less energy consumption means longer working hours [9]. In practical applications, it is necessary for AUVs and ROVs to meet the requirements of different tasks [10]. In contrast to ROVs and AUVs, ARVs have various control modes and flexible operation modes, making them applicable and extensible in ocean engineering. ARVs normally have two operational modes, i.e., the remotely operated mode and the autonomous-operated mode [11]. In the autonomous-operated mode, ARVs can be used in a wide range of search and monitoring applications. In the remotely operated mode, ARVs can be used for detailed inspection and simple maintenance. For the routine maintenance of large offshore engineering projects, such as offshore wind power development, large-scale docks, and marine ranching, the real-time communication and whole-process monitoring of vehicles are essential. The synergy of real-time communication monitoring and autonomous operation in an ARV optimizes its capabilities and broadens its range of applications.

As a new concept of underwater vehicles, research on ARVs is still in the early stages. Some well-known related products include Nereus HROV, Nereid UI, Taser, and Haidou [12]. Nevertheless, similar concepts have been applied and recognized in engineering fields [6,13]. ARVs should be developed while considering the shape design because of their unique energy system [14]. Improved hydrodynamic shapes facilitate the prediction of the hydrodynamic performance of ARVs, thereby reducing the difficulty of control, which makes it possible to engage in more complicated operations for ARVs. The numerous studies on AUVs and ROVs have guiding value for ARV design because of the special operational characteristics and design requirements of ARVs.

The hull shape of underwater vehicles directly affects many important factors, including the structure, general arrangement, vehicle weight, manoeuvrability, etc. Therefore, multidisciplinary and multi-objective optimization designs are more frequently adopted. Multidisciplinary design for disciplinary coupling and multi-objective design for specific requirements have proven that hydrodynamic optimization of underwater vehicle shapes should receive more attention and be developed further. Zhang and Song [15] calculated gradients under a multidisciplinary feasible architecture using the discipline-merging method and obtained the optimized design of a new underwater vehicle. Luo et al. [16] adopted a collaborative optimization method to improve the resistance and manoeuvrability of underwater vehicles. To validate its effectiveness, Hu and Huang [17] presented a multidisciplinary optimization framework that covers multiple disciplines, including the hydrodynamics, structure, and energy requirements, and an AUV was developed based on the results of the proposed framework. As the entire shape optimization process requires a large amount of data to ensure reliability and accuracy, surrogate models and simulation analysis are widely used in small design domains. Furthermore, kriging [18], radial basis functions [19], response surfaces, gene expression programming [20], Artificial Neural Networks (ANNs), and other surrogate models have been applied in the hydrodynamic optimization of underwater vehicles. A dynamic surrogate based on the trust region and lower confidence bound is also a good practice [21]. The application of these methods significantly reduces the computational cost of hydrodynamic simulation and lays the foundation for the rapid and efficient shape design of underwater vehicles. Genetic algorithms and ANN algorithms are widely applied in relevant fields. Wu et al. [22] proposed an improved genetic collision avoidance algorithm to address the problem of Autonomous Surface Vehicles (ASVs) in congested sea areas. ANN models have demonstrated excellent performance in predicting the resistance of ships [23–25].

Furthermore, underwater vehicles are affected by various dynamic loads during operation. This situation is more prominent when working in shallow water. Moreover, the effects of waves and currents should not be overlooked during the design of underwater vehicles. Some scholars have made contributions to related research. Joseph et al. [26] measured the wave-induced forces and moments on various cross-sectional shapes experimentally and found that the heaving force of the revolution body was much smaller than that of the

square and asymmetric structures in most cases. Alvarez et al. [27] investigated the optimum hull shape of an underwater vehicle moving near a free surface and obtained the wave resistance of the revolution body using a first-order Rankine panel method. Shariati et al. [28] studied the effect of appendages on the hydrodynamic characteristics of an underwater vehicle near a free surface and concluded that appendages significantly increase the total resistance. Improvements in shape optimization can reduce wave-induced loads and resistance, which is important for underwater vehicles.

The purpose of this paper is to study the optimization of the shape of an ARV for improving the hydrodynamic performance without an initial model. Based on the characteristics of the objective function and data composition in the design process, an optimization process combining multiple surrogate models is adopted to strike a balance among the data volume, prediction accuracy, and stability. The Pareto solution frontier for waves and yawing conditions is obtained by tending towards small dimensionless forces ($G(x)$) and a larger volume (V). Dimensionless objective values are adopted for comparison to confirm that the method has good engineering applicability. The core of the optimization process is completed by open-source code. The remainder of this paper is organized as follows. In the second section, the design principles and methods employed are introduced. In the third section, details on the simulation calculations and verification are provided. In the fourth section, the complete design optimization process is presented. Finally, conclusions are provided in the last section.

2. Hydrodynamic optimization of the ARV shape

2.1 Design requirement

2.1.1   Design principles

The ARV operation system consists of three parts, namely, the ARV body, the free surface co-module, and the information processing centre, as shown in Figure 1. The ARV and the free surface co-module form a complete operation framework that is connected by a cable. Cables are still an economical and reliable choice for operational depth and underwater communication considerations. The free surface co-module includes necessary parts such as communications devices and main power, while the configuration of the ARV is similar to that of ROVs. In particular, certain measures are essential for an ARV, including a distinct backup power module. The ARV operation system can be used to perform tasks under different work requirements. Moreover, optimizing the shapes of ARVs to improve their hydrodynamic performance is important for ARVs.
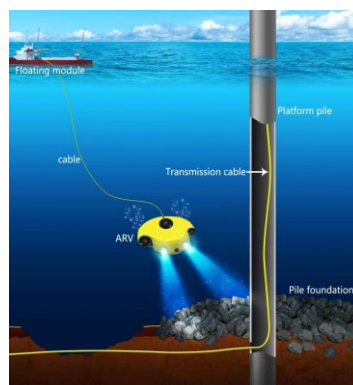
Fig. 1 The prototype of the ARV concept

ARVs have the advantages of two control modes, and the following factors must be considered during their design process:

- Adjustable speed;
- Larger monitoring area;
- Longer working hours;

- Control performance;
- Carrying capacity.

A better hydrodynamic performance is the foundation for achieving the above goals.

2.1.2 The conditions of the sea zones

According to the environmental parameters monitored in a particular offshore wind farm in the South China Sea, the corresponding conditions were specified as the design basis, as shown in Table 1. The data closely resemble the wave data observed without typhoons in the literature [29]. The majority of existing offshore wind farms are located at water depths less than 20 m [30]. Therefore, three typical operating conditions were analysed in detail, with consideration given to the specific marine environment and application. The expected velocity of the ARV was 2 m/s. The detailed parameters of the operating conditions are shown in Table 2. These parameters were utilized to evaluate the hydrodynamic performance of the ARV shape.

Table 1 Environmental parameters of the wind farm

Parameter type	Values
Water depth (m)	20
Annual average significant wave height (m)	0.8
Significant wave period (s)	5.5

Table 2 The parameters of the working conditions

Parameters	Case 1	Case 2	Case 3
Water depth (m)	20	20	20
Wave height (m)	-	0.8	-
Period (s)	-	5.5	-
Operating depth (m)	10	10	10
Wave form	-	Fifth order Stokes wave	-
Relative velocity (m/s)	2	2	2
Yaw angle (°)	0	0	5

2.2 Theoretical methods and models

2.2.1 Artificial Neural Network

ANNs have been widely applied in modern surrogate models, with one advantage being that they consume a trivial amount of computational effort [31]. As an aid to CFD, they greatly improve the optimization efficiency. Their accurate generalization and parallel computation capabilities in complex engineering design problems are helpful in the rapid investigation of the design space [32]. By mimicking the learning process of organisms, ANNs consist of an input layer, one or more hidden layers, and an output layer, each with one or more neurons, in which the computed values are propagated from the input neuron to the output neuron.

The predicted outputs given by the ANN are shown as follows [33]:

$$a^0 = U_i$$

$$\begin{cases} Z^i = W^i a^{i-1} + b^i \\ a^i = H\, Z^i \end{cases} \quad i = 1,\, 2,\, 3\cdots,\, K \tag{1}$$

$$\hat{Y} = W^{K+1} a^K + b^{K+1}$$

where U_i is the input vector, a^i represents the results after the nonlinear mapping of an activation function $H(\cdot)$, Z^i denotes the results after linear mapping for each layer, W^i represents the weight matrices, b^i denotes the bias vectors, and $\hat{Y}$ is the predicted output vector.

2.2.2   Regression Kriging (RK)

The kriging model is an interpolation model with few assumptions, so it has high applicability in many design fields [34,35]. RK is a hybrid interpolation technique that combines regression methods and kriging techniques. Regression is used to fit the explanatory variation, and kriging is used to fit the residuals. RK has a stronger explanatory performance than does ordinary kriging. It can be represented as follows [36]:

$$\hat{z}(s_0) = \hat{m}(s_0) + \hat{e}(s_0)$$

$$\hat{z}(s_0) = \sum_{k=0}^{p} \hat{\beta}_k \cdot q_k(s_0) + \sum_{i=1}^{n} \lambda_i \cdot e(s_i) \tag{2}$$

where $\hat{z}(s_0)$ is the predicted value of the objective variable, $\hat{m}(s_0)$ is the fitted drift, $\hat{e}(s_0)$ is the interpolated residual, $\hat{\beta}_k$ represents the estimated drift model coefficients, λ_i denotes the kriging weights determined by the spatial dependence structure of the residual, and $e(s_i)$ is the residual at location s_i.

2.2.3   Genetic Algorithm (GA)

GAs have been applied in many fields, mimicking the Darwinian theory of the survival of the fittest in nature. The basic elements of GAs are chromosome representation, fitness selection, and biologically inspired operators [37]. GAs have a better global search capability, flexibility, and robustness. They can adjust the encoding, selection, crossover, and mutation combined with engineering requirements, so they are popular in engineering applications.

2.3 Preliminary design and design logic

2.3.1   Shape structure and constraints

The preliminary shape was designed based on the principles of streamline shape designs. It consists of a head, body, and tail, which can change the characteristics of different areas of the surrounding flow field to achieve the design goals. The head and tail were constructed using two planar ellipses, and the body parts were connected by spline curves. The preliminary shape is a conceptual model class rather than an initial model with clear parameters. This will enhance the possibility of our optimization while also increasing its complexity. The parameters of the model are shown in Figure 2, where the blue coordinate system represents the local coordinates of the ARV. The surrogate models took geometric parameters as inputs.

a) Vertical view of the ARV   b) Side view of the ARV

c) Three-dimensional view of the ARV
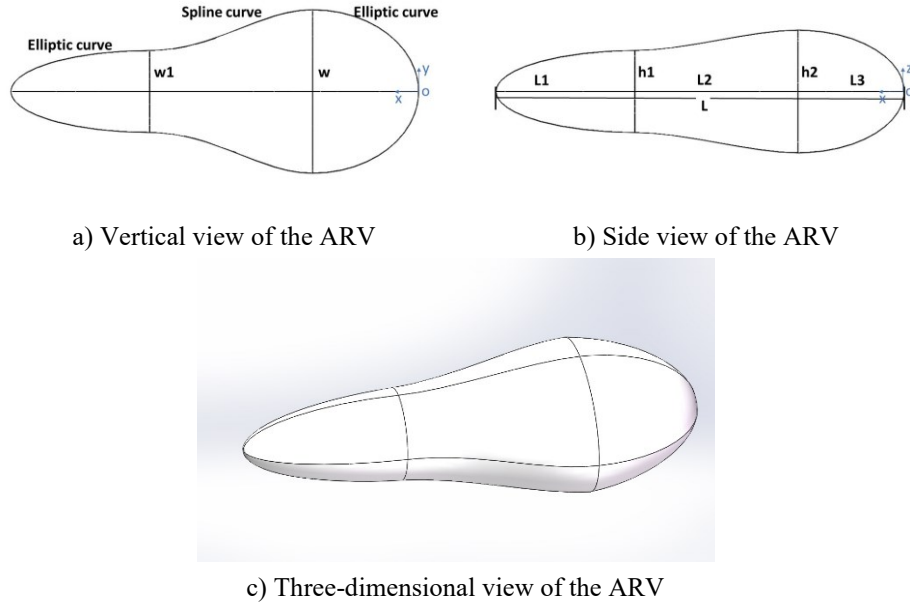
Fig. 2 The detailed diagram of the ARV model parameters

The relationships among the parameters are as follows:

$$\begin{cases} L1+L2+L3 = L = 0.5\,\mathrm{m} \\ 0.05\,\mathrm{m} < L1 < 0.2\,\mathrm{m} \\ 0.05\,\mathrm{m} < L2 < 0.2\,\mathrm{m} \\ 0.05\,\mathrm{m} < w1 < w = 0.15\,\mathrm{m} \\ 0.05\,\mathrm{m} < h1 < h2 \leq 0.15\,\mathrm{m} \end{cases} \tag{3}$$

2.3.2 Optimization problem description

Considering the operation characteristics of shallow water vehicles and the design principle of ARVs, the forces and moments were selected as important references for measuring the hydrodynamic performance. At the same time, several typical operating conditions were analysed to ensure that the designed ARV shape still had good practical value in the real situation of shallow water operation. The dimensionless forces and moments are expressed as follows:

$$G(x) = \frac{1}{\rho g V} \begin{bmatrix} f_r(x) & 0 & 0 \\ 0 & f_h(x) & f_s(x) \\ 0 & \dfrac{M_p(x)}{L} & \dfrac{M_y(x)}{L} \end{bmatrix} \begin{bmatrix} c_s \\ c_w \\ c_y \end{bmatrix} = \begin{bmatrix} F_r \\ F \\ M \end{bmatrix} \tag{4}$$

where $f_r(x)$ denotes the resistance of an ARV while sailing along the x-axis (Case 1). $f_h(x)$ and $M_p(x)$ represent the heaving force and pitching moment, respectively, under wave conditions (Case 2). $f_s(x)$ and $M_y(x)$ represent the transverse force and yawing moment, respectively, under yawing conditions (Case 3). Moreover, the moment centre is chosen at the top of the tail. Table 2 provides detailed information on the operating conditions of the ARV. c_s, c_w and c_y are the weights under different operating conditions, all of which were set to 1 in this paper. Obviously, the water density ρ, gravitational acceleration g, and maximum length L are constants, so $G(x)$ can be regarded as a combination of the unit volume force performance, which is helpful for evaluating the real hydrodynamic performance of the shape of the ARV. A larger cabin means a higher carrying capacity, and it can provide favourable conditions for the modular design of ARVs to

accommodate multiple monitoring and operation requirements. Therefore, *minG(x)* and *maxV* were chosen as the optimization functions. F_r is the dimensionless resistance. F denotes the scalar sum of dimensionless heaving and transverse forces, and M signifies the scalar sum of dimensionless pitching and yawing moments. They were utilized to assess the hydrodynamic performance of the ARV shape under various operating conditions.

2.3.3   Optimization process

The whole optimization process of the ARV shape design was divided into two parts. The initial step was to reduce the design domain based on the core performance. The second step involved establishing a high-fidelity surrogate model under multiple operating conditions and obtaining the Pareto optimal solutions.

A. Reducing the design domain based on core performance

The large design domain increases the possible design choices of ARVs. However, this approach also involves a large number of design variables and high computational costs. Thus, this approach was not worthwhile especially for some abnormally designed candidates, so the preliminary selection of a large design domain was necessary. The large design domain in this paper encompassed all the models that met the length constraint requirement. The difficulty of large design domains is balancing sample data costs, component data sparsity, and model reliability. ANNs are suitable for predicting large-scale and highly complex models [31]. ANNs and GAs were used together in this part. The data samples were supplemented by regions in batches using the optimal Latin hypercube sampling method, which conformed to minimizing the predictor. This approach could not only add as little sample data as possible but also present local gradient changes in real data to a greater extent. A more accurate surrogate model with as few computational costs as possible was built. Therefore, an improved design domain was obtained. This stage required a large amount of data, so we considered only the performance of a single core. In this stage, the hydrodynamic performance ($G(x)$) in Case 1 was evaluated as the core performance and the minimized $G(x)$ value in Case 1 was regarded as the optimization criterion. The data obtained through steady-state calculations were utilized to train and test the ANN surrogate models. The geometrical parameters of the shape models were the inputs of the ANN, while the values of core performance ($G(x)$ in Case 1) of the shape models were the outputs of the ANN.

B. Establishing a high-fidelity surrogate model under multiple operating conditions

After Stage A, the improved design region was generally small, and the unknown objective functions could be considered random continuous distributions. Considering their distribution characteristics, the kriging model was used to predict the objective function. In this stage, typical operating conditions such as shallow water waves were considered. The focus of this stage is on evaluating the hydrodynamic performances ($G(x)$) in Cases 2 and 3, which were determined via unsteady calculations. Finally, Pareto optimal solutions were obtained to ensure better overall performance of the vehicle body.

The entire design logic process is shown in Figure 3.
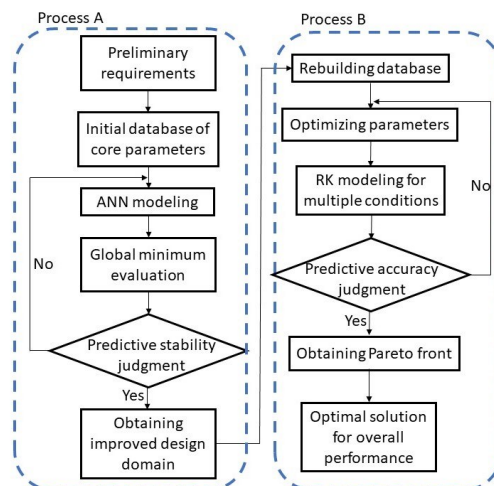
Fig. 3 Optimization process

Notably, the algorithm implementation and data extraction were conducted in Python, the geometric models were generated via SolidWorks, and STAR-CCM+ was used to obtain the hydrodynamic performance as the training and test data for the predictive models. The core of optimization was developed in open-source code, and the entire framework had good scalability and portability.

3. Numerical calculation of the hydrodynamic performance

3.1 Computational domain and boundary conditions

The computational domain was selected and adjusted according to Reference [38]. The inlet boundary was positioned 2.5 L upstream from the top of the head, and the outlet was located 6.5 L downstream. The side boundary was 3 L from the central axis of the vehicle, which was set as a symmetry plane. The surface of the vehicle was set as a non-slip wall. The details of the computational domain are shown in Figure 4. Notably, the results were compared with those of a larger computing domain (1.5 times the side length), and the difference between them was less than 2%. Therefore, the selection of the computational domain was reasonable.

Furthermore, the upper and lower boundaries as well as the inlet were set to vary with changes in the Stokes wave pressure and velocity to simplify the effects of waves. Therefore, the changes in the flow velocity and pressure at the boundary can be simulated. Given the working depth of the ARV, this simplification was necessary.
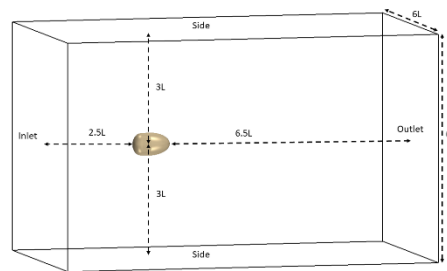
Fig. 4 The computational domain

3.2 Hydrodynamic model, grid, and grid independence study

The computational model was based on the Reynolds Averaged Navier–Stokes (RANS) equations. The finite volume method of the separated flow solver was used to solve the three-dimensional viscous flow field. The k-ω shear stress transport (SST) turbulence model was adopted in this paper. This model accurately resembles actual situations. Thus, it has become the model used by many scholars [9,17]. The pressure-velocity coupling was based on the SIMPLE (Semi-Implicit Method for Pressure-Linked Equation) algorithm. And the second order upwind scheme was used for the spatial discretization of the momentum equations. The convergence criterion of the steady calculation was {RMS} < 1e-6, and the maximum number of iteration steps was set to 1500. In unsteady calculations, the criteria are as follows: {RMS} < 1e-5, a constant time step of 0.02 s and a maximum number of time steps of 150. Additionally, the maximum number of iterations per time step was 10. Notably, the maximum time step in the wave conditions was set at twice the period.

In this study, trimmed meshing is employed with a prism layer. The ARV surface mesh was mainly composed of rectangular elements with some unstructured meshing. The meshing was segmented into zones, with finer mesh sizes near the model surface. This method can ensure the computational economy of the grid construction method. The grid was generated as shown in Figure 5. The y plus for the first layer of the elements from the ARV shape was less than 3.

a) Global meshing   b) Local meshing of the boundary layer
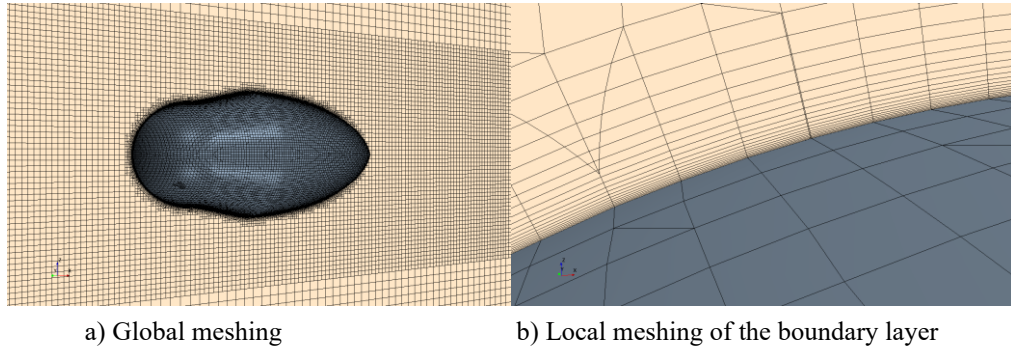
Fig. 5 Meshing

One of the best models in the database was utilized for grid independence analysis. Four grid configurations were systematically generated to study grid independence. The specific parameters of the grids are shown in Table 3. They were studied at a current of 2 m/s.

Table 3 Grid data for grid independence

Parameters	Grid 1	Grid 2	Grid 3	Grid 4
Total cells	1.08e+6	1.39e+6	1.79e+6	2.30e+6
Expansion ratio	1.3	1.3	1.3	1.3
Number of prismatic layers	20	20	20	20
Prismatic layer near wall Thickness (m)	5e-5	5e-5	5e-5	5e-5
Grid refinement factor	-	1.29	1.29	1.29

As shown in Figure 6, the resistance decreased with mesh refinement. From Grid 2 to Grid 3, the deviation in the calculation result was approximately 3%, which indicated that the calculation results were reliable. The calculation equation for the resistance difference ratio $R_{(i,i+1)}$ is as follows:

$$R_{i,i+1} = \frac{Ft_i - Ft_{i+1}}{Ft_{i+1}} \tag{5}$$

where Ft_i is the resistance calculated from Grid i.
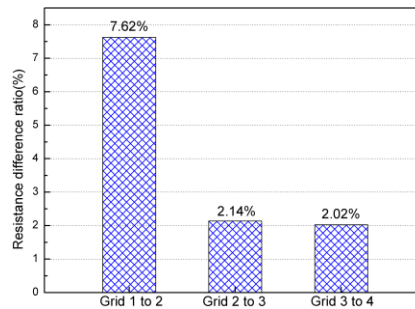
Fig. 6 Variation in the resistance difference ratio with mesh refinement from Grids 1 to 4

3.3 Verification and validation

Due to the challenges presented by large design domains, two models were chosen for verification and validation analyses. Model 1 represented the model with better hydrodynamic performance in the database, while Model 2 represented the model with average hydrodynamic performance in the database. The scale models are depicted in Figure 7.

The grid Convergence Index (GCI) method is known to be an acceptable and recommended method for the estimation of discretization errors in CFD simulations [39]. Model 1 in Case 1 was utilized for GCI

verification, Table 4. Grid 2, Grid 3, and Grid 4 were used for verification by the GCI. Finally, considering error and computational convergence, Grid 3 was selected for analysis.

Table 4 The results of the grid independence simulation

Parameters	Values
r_{32}	1.29
r_{43}	1.29
ϕ_2	6.69
ϕ_3	6.55
ϕ_4	6.42
p_a	3.69
ϕ_{ext}^{32}	6.78
GCI_{fine}^{32}	1.71%

Models 1 and 2 were utilized in scaled wind tunnel experiments to verify the resistance force without any yawing angle. The scaling ratio was 1:5. The experiment was conducted in a wind tunnel, as shown in Figure 7. The detailed parameters are shown in Table 5. The Reynolds number range for the wind tunnel experiments was 5.80e4 to 1.16e5. The same grid settings were scaled according to the characteristic length ratio, which was applied to the wind tunnel model. A comparison between the simulation and experimental results is shown in Figure 8, which reveals that the simulation results were consistent with the experimental results. It was evident that the boundary layer variations and the flow field distribution could be accurately represented by grid division. The same operation was applied for the validation of the suboff model, and the experimental data were obtained from [40]. The suboff model is a structure with typical streamline shape characteristics that has been widely used by scholars for optimization and validation. The Reynolds number range in the suboff model experiments was 3.36e6 to 9.07e6. The errors between the simulation results and experiments were less than 5%, as shown in Figure 9. When the boundary layer variations and flow field distribution can be accurately represented by grid division, the cases still have a good predictive ability in a large Reynolds range.

The validation study of wave-induced loads is based on the experimental data from [41]. The body used for wave testing was an 11.43 cm diameter circular cylinder with hemispheric end caps and a total length of 1.143 m. Moreover, the parameters for the wave experiments are presented in Table 6. The same grid settings were scaled according to the characteristic length ratio for wave validation. Considering the differences in the length-to-width ratios of the models, the computational domain was intentionally reduced below the free surface, and satisfactory results could still be obtained via simulation. A comparison of the experimental and simulation results is shown in Figure 10.

The comparison results validated that the CFD simulation could produce reliable and accurate solutions. Notably, comparisons between the simulation cases with time steps of 0.02 s and 0.005 s were carried out as part of the validation and verification study. It is evident from Figures 8, 9, and 10 that the results of both were essentially the same. The time step was set to 0.02 s due to accuracy and computing resource considerations.

Fig. 7 The wind tunnel experiment

Table 5 The parameters of the wind tunnel

Parameters	Values
Overall dimension (m)	4.55*1.4*1.9
Experimental area (mm)	400*300*700
Maximum wind speed (m/s)	35
Wind speed error (m/s)	±0.15
Test force error (N)	±0.01
Turbulence intensity	<1%

Table 6 The parameters of the wave experiments

Parameters	Values
Section radius (m)	0.05715
Total length of the model, L (m)	1.143
Wave height (m)	0.0508
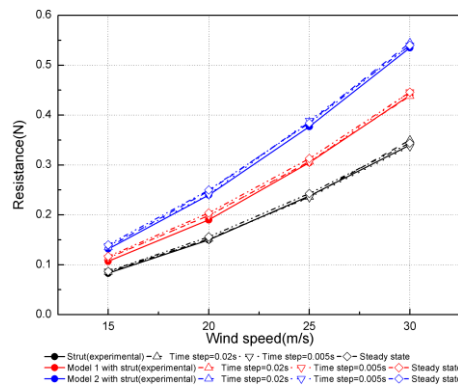
Fig. 8 Comparison of the experimental and calculated values in the wind tunnel
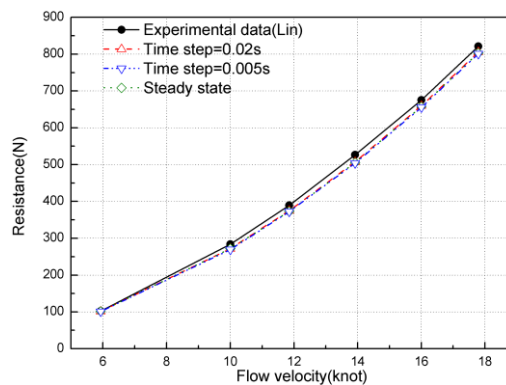
Fig. 9 Comparison of the experimental and calculated values for the suboff model
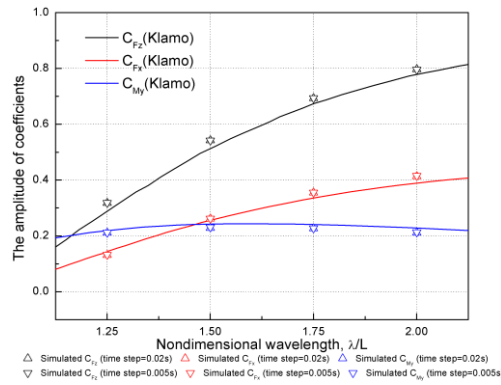
Fig. 10 Comparison of the wave experiments and simulation results

Notes: In the table, C_{F_z} represents the wave-induced maximum heaving force coefficient, C_{F_x} represents the wave-induced maximum resistance coefficient, and C_{M_y} represents the wave-induced maximum pitching moment coefficient.

4. Results and discussion

4.1 Reducing the design domain

In this part of our study, we aimed to obtain an improved design domain with lower costs. Therefore, considering the resistance of the vehicle body as the core performance was acceptable for autonomous systems such as ARVs. The dimensionless force ($G(x)$) calculated from the steady-state simulation in Case 1 was utilized to assess the hydrodynamic performance of the ARV shape.

The initial data size was 300. To minimize the predictor principle, the sample data were added 28 times. It is worth emphasizing that three methods were adopted to prevent the results from converging to local optima. The minimum and suboptimal points were obtained through multiple GA searches, and samples were taken 10 times around each point. The data sampling range adopted the gradually decreasing selection strategy. Data points in the random regions outside the optimal region were added. The final dataset size was 920, and the optimal value could be stabilized within the improved domain.
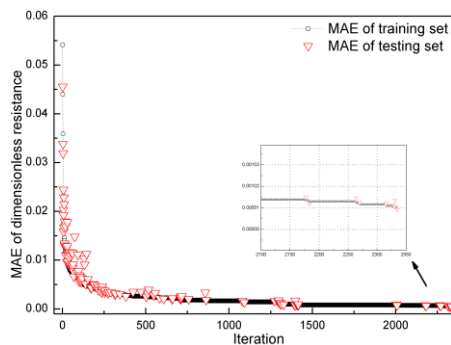
Fig. 11 Convergence history of ANN training
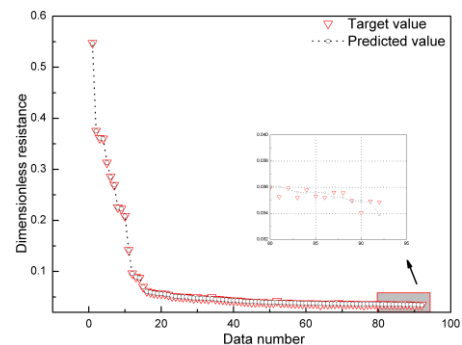
Fig. 12 Comparison between the predicted and objective values

Considering the possible subsequent data expansion, the numbers of hidden layers and nodes were determined. The ANN model had five hidden layers, each layer had 60 neurons, and the activation function was the Exponential Linear Unit (ELU). The output layer did not specify an activation function. The optimizer in the ANN model was Nadam, which combines the Nesterov Accelerated Gradient (NAG) and Adaptive Moment estimation (Adam). The learning rates were adaptive. The settings gave the ANN model good predictive performance in predicting resistance. Training was halted when the mean absolute error (MAE) of the dimensionless force was less than 5.1e-4, with a resulting resistance error of approximately 0.1 N. There was not much hyperparameter optimization performed in this part, despite comparing various settings.

However, these were futile before an improved design domain was obtained. Due to the unique data structure resulting from the supplementary law, a randomly selected 10% of the data was considered to be the test set. Figure 11 displays the variations in the MAEs for both the training and test datasets during the training of the ANN model. The MAEs of both the training and test sets were stable within an acceptable range. Because the supplemented data can be used to satisfactorily minimize the predictor, the model had a greater ability to improve the design domain, as shown in Figure 12.

The improved design domain was determined by the combination of GA searches and simulation data. The predictive performance of the trained ANN model remains consistent after multiple data additions, and the results of the GA searches approached the actual optimal solution domain. These findings implied that the ANN model adeptly captured the resistance, aligning with our expectations in this stage. Using this method, an improved design domain was established with a range of 10 mm, and the details of its centre are shown in Table 7. Figure 13 illustrates the Euclidean metric graph, depicting the relationship between the centre of the improved domain and the results during the last five GA searches. All the last five search results fell within the improved design domain. It is worth noting that the GA integer search was employed in this paper, which partly mitigated the risk of encountering local minimums and enhanced the search efficiency. In the GA integer search, the population size was 200, the number of iterations was 50, the selection operation was tournament selection, and the crossover factor and mutation factor were both 0.5.
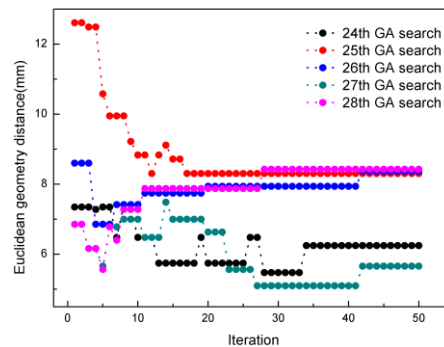
Fig. 13 The convergence process of the GA search

Table 7 The details of the improved design domain

Parameters	Values
$L1$(mm)	80
$L2$(mm)	70
$h1$(mm)	115
$h2$(mm)	140
$w1$(mm)	145

4.2 Establishing the surrogate model

Waves and small-angle disturbances are inherent challenges for shallow underwater vehicles. One hundred sets of data on the hydrodynamic performance of the ARV body under Case 2 and Case 3 were used to establish the surrogate model, and these data were obtained from the simulation cases. In contrast to Stage A, the focus of Stage B is mainly on the accurate predictive ability of the model. The regression model in the RK model adopts support vector regression. A random search approach was employed to optimize the support vector regression and enhance the prediction accuracy of the RK model. Moreover, the predictive coefficient of determination (R^2) was employed to evaluate the confidence of the surrogate models. This validation method analysed the correlation between the surrogate model outputs and expected outputs. Ten percent of the data were utilized for validation purposes. The R2 values for each surrogate model validation are presented in Table 8. In the table, F_z and M_y denote the peak heaving force and pitching moment during a single cycle in Case 2. F_y and M_z represent the transverse force and yawing moment, respectively, in Case 3. V represents

the volume of the model. The reference coordinates and origin are depicted in Figure 2. All R^2 values exceeded 95%, validating the surrogate model's robust adaptability and precise prediction performance across various prediction targets.

Table 8 R^2 values for each prediction target

Prediction target	The values of R^2
F_z	97.2
M_y	99.3
F_y	96.5
M_z	97.2
V	98.2

a) Error analysis of F_z b) Error analysis of M_y

c) Error analysis of F_y d) Error analysis of M_z

e) Error analysis of $V(\mathrm{m}^3)$
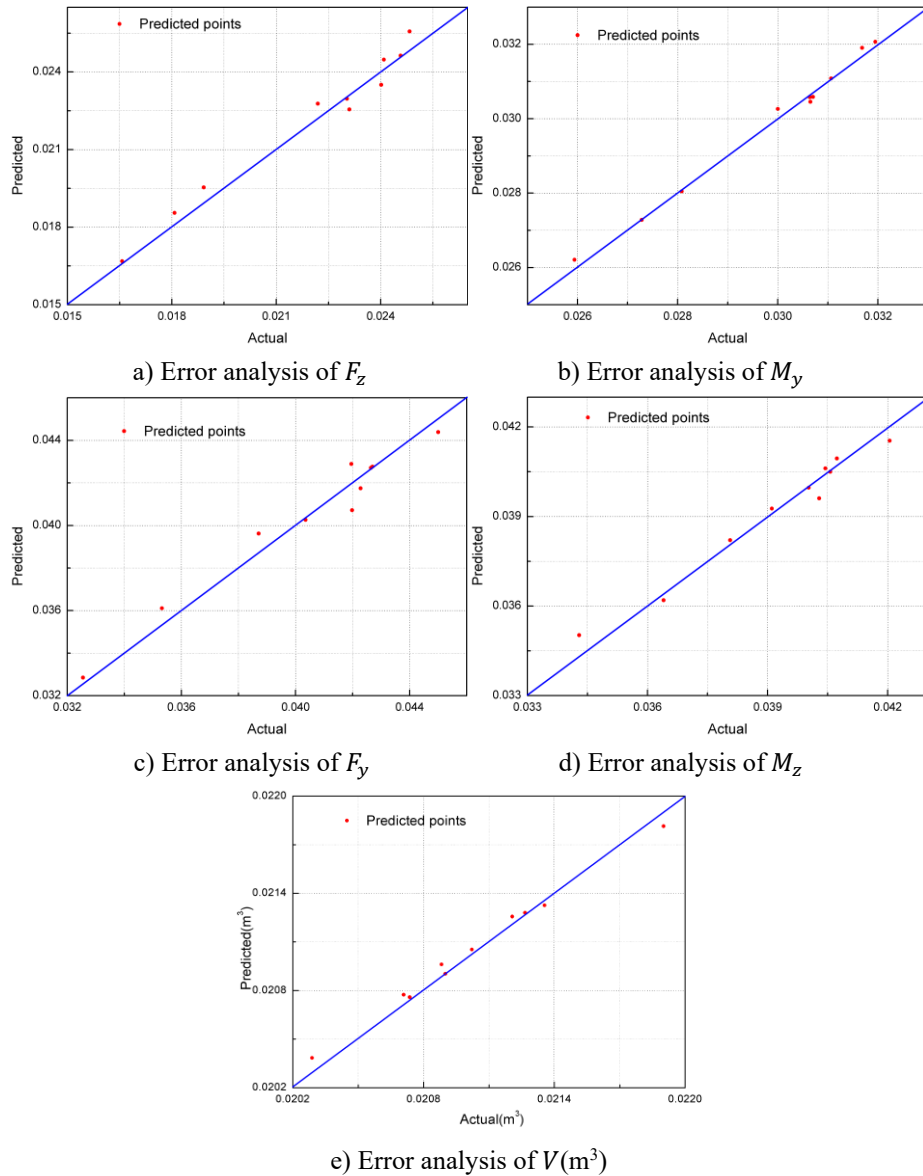
Fig. 14 Error analysis of the prediction targets

Figure 14 shows the predicted results obtained by the surrogate model in comparison with the test data. The maximum relative error occurred at F_z in Case 2, with a value of 3.29%. The maximum absolute error observed in Case 3 for the F_y parameter was approximately 1.27e-3, which corresponded to a transverse force

of approximately 0.25 N. The predicted values agreed well with the test data, proving that the surrogate models have high prediction accuracy and strong generalizability.

| a. Scatter plot of the Pareto frontier | b. X-Z projection plane | c. Y-Z projection plane |
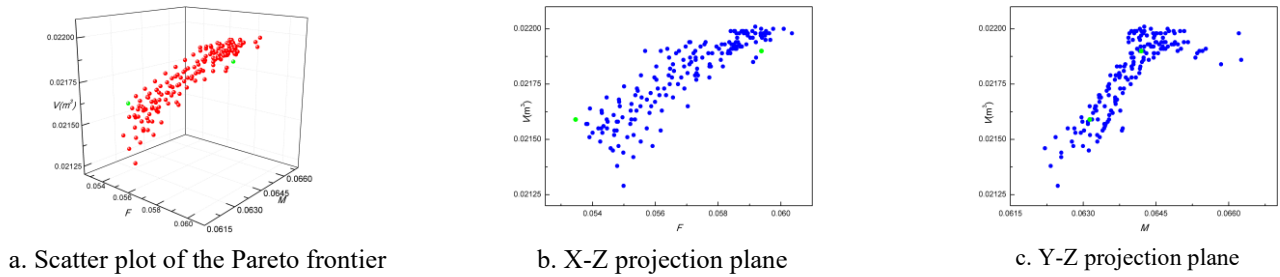
Fig. 15 Pareto optimal solution for the stability and carrying capacity of the vehicle body

Table 9 The comparison between predicted targets by the RK model and simulation results

Parameters	Solution 1	Solution 2	Solution 3	Solution 4
$L1$(mm)	76	75	75	85
$L2$(mm)	70	75	65	75
$h1$(mm)	110	115	110	120
$h2$(mm)	145	145	135	145
$w1$(mm)	150	150	150	150
F	0.05441	0.05754	0.05837	0.06557
Predicted$F$	0.05346	0.05938	0.05734	0.06595
F error (%)	-1.75	3.19	-1.77	0.58
M	0.06228	0.06359	0.06547	0.06674
Predicted$M$	0.06313	0.06419	0.06535	0.06842
M error (%)	1.38	0.95	-0.19	2.52
V (m^3)	0.02174	0.02202	0.02043	0.02214
Predicted V (m^3)	0.02159	0.0219	0.02061	0.02186
V error (%)	-0.69	-0.54	0.88	-1.26

Notes: In the table, F denotes the scalar sum of dimensionless heaving and transverse forces, and M signifies the scalar sum of dimensionless pitching and yawing moments.

The Pareto optimal solution is a crucial concept in multi-objective optimization problems because it represents the optimal trade-off point for balancing diverse objectives. In the design of small ARVs in shallow water, the stability, control ability, and carrying capacity are crucial performance factors. Hence, it is necessary to more fully consider the overall performance during the design process. For the sake of visual presentation, the forces and moments under Case 2 and Case 3 were combined separately to create a Pareto solution frontier that encompassed dimensionless forces (F), dimensionless moments (M), and volumes. The Pareto solutions tend towards a small dimensionless force, a small dimensionless moment, and a large volume. The technique of combining the NSGA-II and GA integer search was employed, and the Pareto solution frontier was ultimately obtained after 50 iterations, as depicted in Figure 15. In the ideal Pareto solution set of the improved design domain, the variation in the range of F was the largest, at greater than 12%. M exhibited a variation range exceeding 6.5%. The change in the vehicle volume was less than 3.5%. It should be noted that there was a substantial range of variability in the moment and volume during the simulation and RK models of 13% and 8%, respectively, providing ample space for candidate solutions. Considering the Pareto frontier and the improved design domain, four representative solutions were chosen for comparison with the predicted values of the RK model. Solutions 1 and 2 were the points on the Pareto frontier. Solution 1 had the lowest predicted

value of F, while Solution 2 had a higher predicted value of F. They are depicted as green dots in Figure 15. The parameters in Solution 3 were the minimum values that could be achieved for all the parameters except $w1$ in the improved design domain. In contrast, those in Solution 4 were the maximum values. The results are shown in Table 9. By verifying these shape models, it was evident that the RK model had a high prediction accuracy near the Pareto frontier and over the improved design domain.

4.3 Performance analysis of the optimization results

The models on the boundaries of the improved design are represented by Solutions 3 and 4. Solution 1 represents the better overall performance model. More details of Solutions 1, 3 and 4 were compared. The outcomes of these analyses have significant reference value for design purposes.

Figure 16 is the comparison diagram (on the XOZ plane) of flow field details during the moment of maximum heaving force experienced by the model in Case 2, where the velocity vector fields are presented using the line integral convolutions. The three models consistently showed a flow field distribution with a higher fluid velocity along the spline positioned on the upper and lower sides. Among them, the flow velocity transition in Figure 16(c) is more gradual, with a reduced difference between the upper and lower surface flow velocities, leading to a decreased level of wave-induced force in Case 2. The flow velocity at Point A in Figure 16(a) was lower, and the distance between Points A and B was greater, resulting in a weakened influence between them. Consequently, the flow velocity influence area depicted in Figure 16(a) was smaller than that in Figure 16(b). The variation in height will inevitably impact the location of the separation point. Moreover, due to the nature of wave motion, relying on the separation point as a definitive reference for analysis is not feasible.

| a) Model of Solution 1 | b) Model of Solution 3 | c) Model of Solution 4 |
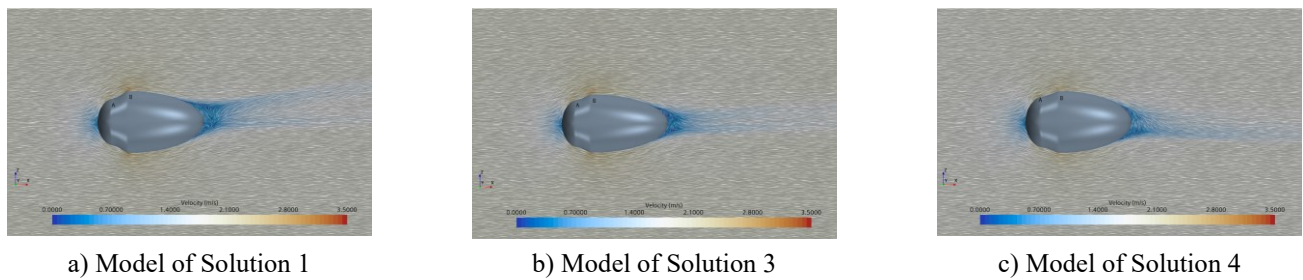
Fig. 16 The comparison of the flow field details in Case 2

| a) Model of Solution 1 | b) Model of Solution 3 | c) Model of Solution 4 |
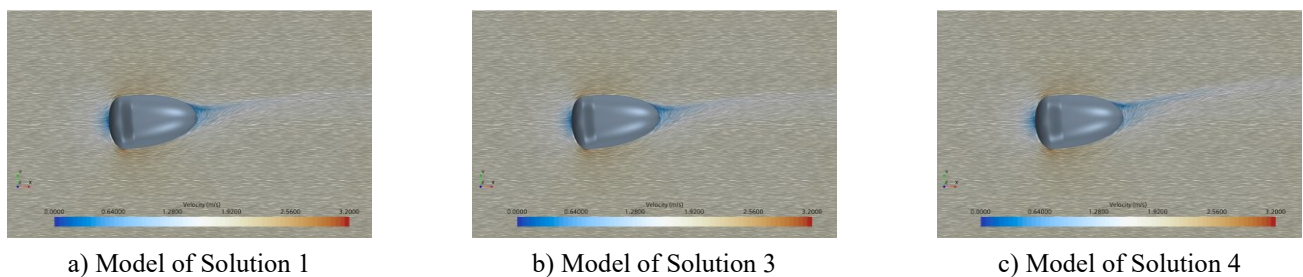
Fig. 17 The comparison of the flow field details in Case 3

Figure 17 shows a comparison diagram of the flow field details in the XOY plane obtained by the model for Case 3. The transverse force in the local coordinate system of the model was a combination of axial forces in the x and y directions in the global coordinate system. The flow field distributions on both sides of the three models were essentially the same. However, the projected area in the XOZ plane in the local coordinate system decreased in the following order: Solutions 4, 1, and 3. The fluid separation point was moved forward in Figure 17(c), resulting in a larger wake area. Considering both factors, the transverse forces in the local coordinate system exhibited an increasing order as follows: Solutions 3, 1, and 4.

5. Conclusions

In this study, a multi-surrogate model approach was employed to optimize the hydrodynamic performance of an ARV shape without an initial model. To enhance the engineering applicability of our

method, dimensionless objective values were used. The programming is based on open-source code, making the entire process highly extensible, transparent, and applicable for further research.

The optimal Latin hypercube sampling technique was applied to construct the original dataset for the ANN surrogate model. By employing a GA integer search and the principle of the minimum prediction factor, the ANN surrogate model was progressively enhanced and expanded. After multiple iterations and updates, the ANN surrogate model can reliably predict global trends to obtain an improved design domain. RK models based on a support vector product were then constructed to improve the spatial correlation of the data and minimize data requirements. The RK models exhibited excellent applicability under various operating conditions.

Within the improved design domain, we focused on the multi-objective optimization of hydrodynamic performance. The Pareto frontier of the optimized design domain was obtained through the application of the NSGA-II algorithm and a GA integer search. The optimization results are consistent with the simulation results, confirming the effectiveness and reliability of the optimization process. In the Pareto frontier solution, the variation in the range of force F is greater than 12%, M exhibits a variation range exceeding 6.5%, and the change in the vehicle's volume is less than 3.5%. Therefore, engineering requirements should be developed to place more emphasis on the design and optimization of the overall performance.

This study confirmed the design and optimization process of the hydrodynamic shape of an ARV. Future research will focus on the optimization of hydrodynamic performance and the principle of underwater vehicles in more complex situations. Furthermore, the authors will also focus on creating a system that provides a more overall evaluation of the performance of underwater vehicles.

6. Acknowledgements

REFERENCES

[1]   Shukla, A., Karki, H., 2016. Application of Robotics in Offshore Oil and Gas Industry-A Review Part II. *Robotics and Autonomous Systems*, 75, 508–524. https://doi.org/10.1016/j.robot.2015.09.013

[2]   Capocci, R., Dooly, G., Omerdić, E., Coleman, J., Newe, T., Toal, D., 2017. Inspection-Class Remotely Operated Vehicles-a Review. *Journal of Marine Science and Engineering*, 5(1). https://doi.org/10.3390/jmse5010013

[3]   Khawaja, W., Semkin, V., Ratyal, N.I., Yaqoob, Q., Gul, J., Guvenc, I., 2022. Threats from and Countermeasures for Unmanned Aerial and Underwater Vehicles. *Sensors*, 22, 1–30. https://doi.org/10.3390/s22103896

[4]   He, Y., Wang, D.B., Ali, Z.A., 2020. A Review of Different Designs and Control Models of Remotely Operated Underwater Vehicle. *Measurement and Control (United Kingdom)*, 53, 1561–1570. https://doi.org/10.1177/0020294020952483

[5]   Deep-Sea Scientific Investigation and Manned Submersible Technology. *Bulletin of the Chinese Academy of Sciences*, 34, 34–36, 2020. https://doi.org/10.3724/SP.J.7101866527

[6]   Bowen, A.D., Yoerger, D.R., Whitcomb, L.L., Fornari, D.J., 2004. Exploring the Deepest Depths: Preliminary Design of a Novel Light-Tethered Hybrid ROV for Global Science in Extreme Environments. *Marine Technology Society Journal*, 38, 92–101. https://doi.org/10.4031/002533204787522776

[7]   Javaid, M.Y., Ovinis, M., Nagarajan, T., Hashim, F.B.M., 2014. Underwater Gliders: A Review. *4th International Conference on Production, Energy and Reliability, ICPER 2014*, 3-5 June, Kuala Lumpur, Malaysia, 13, 1–5. https://doi.org/10.1051/matecconf/20141302020

[8]   Panda, J.P., Mitra, A., Warrior, H. V., 2021. A Review on the Hydrodynamic Characteristics of Autonomous Underwater Vehicles. *Proceedings of the Institution of Mechanical Engineers Part M: Journal of Engineering for the Maritime Environment*, 235, 15–29. https://doi.org/10.1177/1475090220936896

[9]   Zheng, G., Yang, X., 2018. Studies of the Resistance Optimization of Underwater Vehicle Based on Multiple-Speed Approximate Model. *2nd International Conference on Functional Materials and Chemical Engineering, ICFMCE 2018*, 20-22 November, Abu Dhabi, UAE, 272, 01029. https://doi.org/10.1051/matecconf/201927201029

[10]   Yoerger, D.R., Bradley, A.M., Jakuba, M., German, C.R., Shank, T., Tivey, M., 2007. Remotely Operated Vehicle Technology Exploration, and Sampling. *Oceanography*, 20(1), 152-161. https://doi.org/10.5670/oceanog.2007.89

[11]   Jiang, Z., Lu, B., Wang, B., Cui, W., Zhang, J., Luo, R., Luo, G., Zhang, S., Mao, Z., 2022. A Prototype Design and Sea Trials of an 11,000 m Autonomous and Remotely-Operated Vehicle Dream Chaser. *Journal of Marine Science and Engineering*, 10(6), 812. https://doi.org/10.3390/jmse10060812

[12]   Li, Y., Li, S., Zhang, A., 2016. Research Status of Autonomous & Remotely Operated Vehicle. *Journal of Engineering Studies*, 8, 217–222.

[13]   Khojasteh, D., Kamali, R., 2017. Design and Dynamic Study of a ROV with Application to Oil and Gas Industries of Persian Gulf. *Ocean Engineering*, 136, 18–30. https://doi.org/10.1016/j.oceaneng.2017.03.014

[14]   Tang, Y., Wang, J., Lu, Y., Yao, Z., 2019. Parametric Design Method and Experimental Research on Haidou Full-Depth Ocean Autonomous and Remotely-Operated Vehicle. *Robot*, 41, 697–705.

[15]   Zhang, D., Song, B., Wang, P., Chen, X., 2017. Multidisciplinary Optimization Design of a New Underwater Vehicle with Highly Efficient Gradient Calculation. *Structural and Multidisciplinary Optimization*, 55, 1483–1502. https://doi.org/10.1007/s00158-016-1575-2

[16]   Weilin, L., Taichun, R., 2018. An Approach of Multidisciplinary Optimization to Underwater Vehicle Profile Designs. *8th International Conference on Information Science and Technology, ICIST 2018*, 30 June- 6 July, Granada, Spain, 133–137. https://doi.org/10.1109/ICIST.2018.8426127

[17]   Hu, F., Huang, Y., Xie, Z., Yu, J., Wang, Z., Qiao, J., 2022. Conceptual Design of a Long-Range Autonomous Underwater Vehicle Based on Multidisciplinary Optimization Framework. *Ocean Engineering*, 248, 110684. https://doi.org/10.1016/j.oceaneng.2022.110684

[18]   Dong, H., Song, B., Wang, P., 2016. Surrogate-Based Optimization for Autonomous Underwater Vehicle's Shell Design. *Proceedings of the 14th International Symposium on Distributed Computing and Applications for Business, Engineering and Science, DCABES 2015*, 18-24 August, Guiyang, China, 393–397. https://doi.org/10.1109/DCABES.2015.105

[19]   Zhang, T., Zhou, H., Wang, J., Liu, Z., Xin, J., Pang, Y., 2019. Optimum Design of a Small Intelligent Ocean Exploration Underwater Vehicle. *Ocean Engineering*, 184, 40–58. https://doi.org/10.1016/j.oceaneng.2019.05.015

[20]   Tang, Q., Li, Y., Deng, Z., Chen, D., Guo, R., Huang, H., 2020. Optimal Shape Design of an Autonomous Underwater Vehicle Based on Multi-Objective Particle Swarm Optimization. *Natural Computing*, 19, 733–742. https://doi.org/10.1007/s11047-019-09729-7

[21]   Luo, W., Guo, X., Dai, J., Rao, T., 2021. Hull Optimization of an Underwater Vehicle Based on Dynamic Surrogate Model. *Ocean Engineering*, 230, 109050. https://doi.org/10.1016/j.oceaneng.2021.109050

[22]   Wu, G., Li, Y., Jiang, C., Wang, C., Guo, J., Cheng, R., 2022. Multi-Vessels Collision Avoidance Strategy for Autonomous Surface Vehicles Based on Genetic Algorithm in Congested Port Environment. *Brodogradnja*, 73(3), 69–91. https://doi.org/10.21278/brod73305

[23]   Martić, I., Degiuli, N., Grlj, C.G., 2023. Prediction of Added Resistance of Container Ships in Regular Head Waves Using an Artificial Neural Network. *Journal of Marine Science and Engineering*, 11(7), 1293. https://doi.org/10.3390/jmse11071293

[24]   Martić, I., Degiuli, N., Majetić, D., Farkas, A., 2021. Artificial Neural Network Model for the Evaluation of Added Resistance of Container Ships in Head Waves. *Journal of Marine Science and Engineering*, 9(8), 826. https://doi.org/10.3390/jmse9080826

[25]   Yıldız, B., 2022. Prediction of Residual Resistance of a Trimaran Vessel By Using an Artificial Neural Network. *Brodogradnja*, 73(1), 127–140. https://doi.org/10.21278/brod73107

[26]   Klamo, J.T., Yeager, K.I., Cool, C.Y., Turner, T.M., Kwon, Y.W., The Effects of Cross-Sectional Geometry on Wave-Induced Loads for Underwater Vehicles. IEEE Journal of Oceanic Engineering, 46(3), 765-784. https://doi.org/10.1109/JOE.2020.3023320

[27]   Alvarez, A., Bertram, V., Gualdesi, L., 2009. Hull Hydrodynamic Optimization of Autonomous Underwater Vehicles Operating at Snorkeling Depth. *Ocean Engineering*, 36, 105–112. https://doi.org/10.1016/j.oceaneng.2008.08.006

[28]   Shariati, S.K., Mousavizadegan, S.H., 2017. The Effect of Appendages on the Hydrodynamic Characteristics of an Underwater Vehicle near the Free Surface. *Applied Ocean Research*, 67, 31–43. https://doi.org/10.1016/j.apor.2017.07.001

[29]   Liu, Y., Li, S., Yi, Q., Chen, D., 2017. Wind Profiles and Wave Spectra for Potential Wind Farms in South China Sea. Part II: Wave Spectrum Model. *Energies*, 10(1), 127. https://doi.org/10.3390/en10010127

[30]   Sánchez, S., López-Gutiérrez, J.S., Negro, V., Esteban, M.D., 2019. Foundations in Offshore Wind Farms: Evolution, Characteristics and Range of Use. Analysis of Main Dimensional Parameters in Monopile Foundations. *Journal of Marine Science and Engineering*, 7(12), 441. https://doi.org/10.3390/jmse7120441

[31]   Sun, G., Wang, S., 2019. A Review of the Artificial Neural Network Surrogate Modeling in Aerodynamic Design. *Proceedings of the Institution of Mechanical Engineers, Part G: Journal of Aerospace Engineering*, 233, 5863–5872. https://doi.org/10.1177/0954410019864485

[32]   Van Nguyen, N., Lee, J.W., Tyan, M., Kim, S., 2015. Repetitively Enhanced Neural Networks Method for Complex Engineering Design Optimisation Problems. *Aeronautical Journal*, 119, 1253–1270. https://doi.org/10.1017/S0001924000011234

[33]   He, H.W., Wang, Z.H., Zou, Z.J., Liu, Y., 2022. Nonparametric Modeling of Ship Maneuvering Motion Based on Self-Designed Fully Connected Neural Network. *Ocean Engineering*, 251, 111113. https://doi.org/10.1016/j.oceaneng.2022.111113

[34]   Forrester, A.I.J., Keane, A.J., 2009. Recent Advances in Surrogate-Based Optimization. *Progress in Aerospace Sciences*, 45, 50–79. https://doi.org/10.1016/j.paerosci.2008.11.001

[35]   Hou, S., Zhang, Z., Lian, H., Xing, X., Gong, H., Xu, X., 2022. Hull Shape Optimization of Small Underwater Vehicle Based on Kriging-Based Response Surface Method and Multi-Objective Optimization Algorithm. *Brodogradnja*, 73(3), 111–134. https://doi.org/10.21278/brod73307

[36]   Hengl, T., Heuvelink, G.B.M., Rossiter, D.G., 2007. About Regression-Kriging : From Equations to Case Studies. *Computers & Geosciences*, 33(10), 1301–1315. https://doi.org/10.1016/j.cageo.2007.05.001

[37]   Katoch, S., Chauhan, S.S., Kumar, V., 2021. A Review on Genetic Algorithm: Past, Present, and Future. *Multimedia Tools and Applications*, 80, 8091–8126. https://doi.org/10.1007/s11042-020-10139-6

[38]   Cho, Y.J., Seok, W., Cheon, K.H., Rhee, S.H., 2020. Maneuvering Simulation of an X-Plane Submarine Using Computational Fluid Dynamics. *International Journal of Naval Architecture and Ocean Engineering*, 12, 843–855. https://doi.org/10.1016/j.ijnaoe.2020.10.001

[39]   Javanmard, E., Yari, E., Mehr, J.A., Mansoorzadeh, S., 2019. Hydrodynamic Characteristic Curves and Behavior of Flow around a Surface-Piercing Propeller Using Computational Fluid Dynamics Based on FVM. *Ocean Engineering*, 192, 106445. https://doi.org/10.1016/j.oceaneng.2019.106445

[40]   Lin, Y.H., Li, X.C., 2020. The Investigation of a Sliding Mesh Model for Hydrodynamic Analysis of a Suboff Model in Turbulent Flow Fields. *Journal of Marine Science and Engineering*, 8(10), 744. https://doi.org/10.3390/jmse8100744

[41]   Klamo, J.T., Turner, T.M., Cool, C.Y., Yeager, K.I., Kwon, Y.W., 2021. On the Accuracy of an Analytical Solution to Model Wave-Induced Loads on an Underwater Vehicle in Real-Time. *Journal of Offshore Mechanics and Arctic Engineering*, 143(3), 031202. https://doi.org/10.1115/1.4049119